

# Inversion of the shape of space debris from non-resolved optical measurements within SPOOK

**David Vallverdú Cabrera**

*Airbus DS, 88039 Friedrichshafen, Germany, david.vallverdu\_cabrera@airbus.com*

**Jens Utzmann**

*Airbus DS, 88039 Friedrichshafen, Germany, jens.utzmann@airbus.com*

**Roger Förstner**

*Universität der Bundeswehr München, 85579 Neubiberg, Germany, roger.foerstner@uinbw.de*

## ABSTRACT

Shape characterization for Resident Space Objects (RSO) has been included in the Special Perturbations Orbit determination and Orbit analysis toolKit (SPOOK), a multi-purpose Space Surveillance and Tracking (SST) software framework developed by the Security in Space team at Airbus Defence and Space. The method, explored in the asteroid and the artificial objects characterization communities, estimates the shape of an object from a light curve measurement, and requires the attitude of the RSO, as well as its orbit, to be known *a priori*. It is a two-step process in which first, the Extended Gaussian Image (EGI) of the object is estimated from its light curve; second, the actual shape is reduced from the EGI using Minkowski's minimization. With this addition, SPOOK now has separate attitude (partial) characterization, as well as shape estimation capabilities. For convex objects, the test results on simulated scenarios show that the shapes recovered maintain good fidelity with the truth; non-convex objects yield an *equivalent* convex shape, which is different from the original shape, albeit useful in its own right. Experiments show that, thanks to the positive area constraint, the fact that the problem is unobservable in classical terms does not affect the performance of the shape inversion.

## 1. INTRODUCTION

ESA's Annual Space Environment Report highlights the dangers of the ever increasing space debris population orbiting the Earth. Its growth is now dominated by the surge of mega constellations [4]. The Report calls for immediate action to mitigate the potential impact on current and future missions. This mitigation effort must include proper cataloging, identification and characterization of Resident Space Objects (RSO). *E.g.* Active Debris Removal is likelier to succeed if the shape of the target is known beforehand.

The time series of brightness measurements taken by an optical telescope while tracking a RSO – the RSO's light curve – encode characteristics of the object itself, such as attitude, and shape, along with size and surface reflective properties. Thus, when resolved imagery is not available, light curves are commonly used to characterize space objects. The asteroid community pioneered these kind of techniques [13, 14, 23] which, during the last decade, have been adapted and extended to characterize artificial objects from light curves [6, 10, 17].

With particular focus on shape recovery, Kaasalainen and Torppa [12] developed a method to recover asteroid shapes in a two-step process: first, they extracted an Extended Gaussian Image from the light curve data; then, they recovered the shape itself using Little's work [18], which exploits Minkowski's theorem [19]. Calef *et al.* [3] ported this process to the case of artificial objects, exploring the benefits of ridge regularization. More recently, Fan, Friedman, Früh *et al.* further explored the observability of this method and its stability against measurement noise. They proposed extensions to overcome some of its shortcomings, including the usage of multiple light curves and multiple-hypothesis approach [5–8].

The Security in Space team at Airbus Defence and Space develops the Special Perturbations Orbit determination and Orbit analysis toolKit (SPOOK), a software framework aimed at solving multiple Space Surveillance and Tracking

(SST) problems, including object catalog maintenance and generation, as well as, collision avoidance, sensor simulation and observation planing [20–22]. SPOOK has been recently upgraded with light-curve-based object characterization capabilities [25], which have been enhanced with convex shape determination within the scope of this paper. Thus, this paper can be seen as the second part of the more general push to enable object characterization in SPOOK.

The following section starts by explaining the shape determination algorithm implemented in SPOOK, based on previous literature, and highlighting its most relevant features, constraints and variants. Sec. 3 follows with a description of the simulation scenarios that have been used to test and validate the implementation. The simulation results are then presented and discussed in Sec 4. By the end, Sec. 5 briefly discusses the potential extensions to include albedo, non-convex shapes and attitude estimations to the SPOOK shape inversion pipeline. The paper finishes with the summary and conclusions of the work presented here (Sec. 6).

## 2. SHAPE INVERSION FROM A LIGHT CURVE

This section explains the shape determination algorithm that recovers a convex shape from a light curve. The process is divided in two steps:

1. first, an Extend Gaussian Image (EGI) is estimated from the input light curve;
2. second, a shape, formally represented by a convex polyhedron in 3D, is recovered from the EGI.

The rest of this section is divided into the building blocks of the above process, starting with the EGI to shape step, followed by the light curve model, the light curve to EGI step and the observability conditions of the problem.

### 2.1 EGI to Convex Shape

This sub-section explains how to recover a convex polyhedron, which represents the shape, from a EGI. Thus, it starts by defining what an Extend Gaussian Image is.

#### 2.1.1 Extended Gaussian Images

**Definition 1.** *The **Extended Gaussian Image (EGI)** of a convex 3D object, represented by the closed surface  $O \in \mathbb{R}^3$ , is a map from the Gaussian sphere  $S = \{n \mid \|n\| = 1, n \in \mathbb{R}^3\}$  to the variation of area of  $O$  normal to  $n$  with the area of  $S$  normal to  $n$  [11]. This is*

$$\text{EGI}(n) = \frac{dO}{dS}(n) \quad (1)$$

or area density.

**Corollary 1.** *Let us define a convex polyhedron  $P \in \mathbb{R}^3$  with  $N_f$  flat faces, whose areas and normals  $A_i$  and  $n_i$ , respectively, for  $i \in \{1, \dots, n_{N_f}\}$ . Its EGI can be expressed as*

$$\text{EGI}(n) = \begin{cases} A_i \delta(n) & n \in \{n_1, \dots, N_f\}, \\ 0 & \text{else,} \end{cases} \quad (2)$$

where  $\delta(n)$  is the impulse function on the surface of the Gaussian sphere [11]. This can be compactly described by the set of vectors [18]

$$\text{EGI}(P) = \{A_i n_i \mid i \in \{1, \dots, N_f\}\}. \quad (3)$$

**Theorem 1.** *As proven by Minkowski [19], if*

$$\sum_{i=1}^{N_f} A_i n_i = 0, \quad (4)$$

then the EGI is a unique representation of a convex polyhedron [18].

**Corollary 2.** *The EGI of a polyhedron can be approximated on a fixed set of  $N_a$  directions  $\{n_j | j \in \{1, \dots, N_a\}\}$  on the unit sphere, which may not necessarily coincide with the set of the polyhedron face normals. This is done by associating the out-facing normals of  $P$  to the closest of each of these directions. As a set, this is*

$$\widehat{\text{EGI}}(P) = \left\{ \sum_{i=1}^{N_f} \tau_j(n_i) A_i n_j \mid j \in \{1, \dots, N_a\} \right\}, \quad (5)$$

where  $\tau_j(n)$  is 1 if  $n_j$  is the closest approximation to  $n/\|n\|$  and 0 otherwise. Depending on how  $\tau_j(n)$  is implemented, different definitions of "closest" may be used. Whatever the implementation, it is necessary that  $\sum_j \tau_j(n) = 1$  for any  $n \in \mathbb{R}^3$ .

### 2.1.2 Sphere Tessellation

The tessellation used to generate an EGI in this paper is the same as in [5–8], the quad-cube tessellation [27], in which the 12 edges of a cube are projected onto the sphere as great circle arcs, and then each face is sub-gridded using axial planes rotated at a constant angle from each other. This results in a tessellation composed of similar, approximately squared cells. In this tessellation, the  $\tau_j(n)$  function is defined so that it is 1 only if  $n$  is inside cell  $j$ . The direction  $j$  represented by each cell is the center of the cell when mapped onto a perfect square. Fig. 1 is an example of a quad-cube tessellation where each cube face is sub-divided into a  $5 \times 5$  grid of cells. Generalizing, a quad-cube tessellation whose faces are divided into  $d \times d$  cells each has a total of  $N_a = 6d^2$  cells.

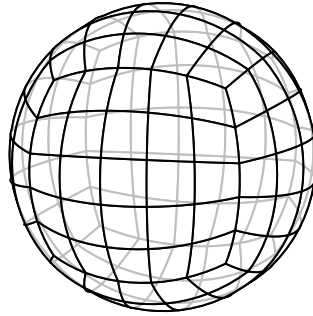


Fig. 1: An example of a quad-cube tessellation with a grid of  $5 \times 5$  cells on each face

### 2.1.3 Generating a Convex Polyhedron from Known Supports

**Definition 2.** *Given a polyhedron in  $\mathbb{R}^3$  with  $N_f$  faces, the **support** [18] of the  $i^{\text{th}}$  face  $F_i$  is defined as*

$$h_i = n_i \cdot x, \forall x \in F_i, \quad (6)$$

where  $n_i$  is the unitary out-facing normal of the plane that contains face  $F_i$ . The  $\cdot$  operator is the dot product.

As described by Little [18], if the list of supports and corresponding unitary normals of a convex polyhedron are known, the vertices, edges and faces of the same can be recovered. First, the list of supports describes the location of all the planes that bind the polyhedron to be recovered. Therefore, it also describes the location of the vertices of the dual of the target polyhedron. Thus, one can obtain the target polyhedron by performing a convex hull of the locations described by the supports as vertices, and then calculating the dual of such hull. The adjacency information can be obtained by interchanging faces and vertices in the adjacency tables (vertices per face and faces per vertex) of the convex hull. This operation can be denoted as the function  $P(h)$ , which obtains the vertices of a polyhedron and its adjacency information from its list of supports  $h \in \mathbb{R}^{N_f}$ .

### 2.1.4 Calculating the Supports of an EGI

Minkowski [19] showed that, for an unknown polyhedron of which only the area and normal of each face are known, the equivalent polyhedron of unit volume can be recovered by solving the minimization problem [18]:

$$\begin{aligned} \min_h \quad & \sum_{i=1}^N h_i A_i, \\ \text{subj. to} \quad & V(P(h)) = 1, \\ & h_i > 0. \end{aligned} \quad (7)$$

The function  $V(P)$  returns the volume of polyhedron  $P$ . The inequality constraint ensures that the origin is always inside the recovered polyhedron. This problem can be solved with modern constrained convex minimization [18], such as the trust-region interior point method [2] employed in this paper.

### 2.2 The Light Curve Model

The shape information of an object is encoded within its light curve, provided it can be observed from a wide enough variety of directions [8]. The light curve can be modeled as the contribution of

$$L = SA, \quad (8)$$

where  $L \in \mathbb{R}^{N_t}$  is the light curve stored as a vector of electron flux measurements<sup>1</sup>;  $A \in \mathbb{R}^{N_a}$  is the vector that contains the  $N_a$  area values of an EGI;  $S \in \mathbb{R}^{N_t \times N_a}$  is the scattering [12] matrix, where each row describes how the light coming from the Sun is reflected on each of the faces of the EGI so that it produces the appropriate measurement in  $L$ , while each column is the electron flux detected from each face per unit of area. Therefore, each row of  $G$  depends in general on the measurement time, on the instantaneous attitude of the modeled object, and on its surface reflective properties and how they can be modeled. These properties must be known for the shape inversion method described here.

For the particular case when all faces of the EGI have the same albedo  $\rho$  (*i.e.* they all reflect the same amount of sunlight at any arbitrary pair of incident and reflected directions) the albedo can be factored out of  $S$  and incorporated into  $A$ , giving rise to the reflection matrix  $G = S/\rho$  [5] and the albedo-area vector  $a = \rho A$ , so that Eq. 8 becomes

$$L = Ga. \quad (9)$$

Note that  $a$  can still be used as the *areas* of an EGI, because isotropic scaling does not invalidate the zero-residual condition imposed by Eq. 4.

In this paper, the matrix  $G$  used assumes Lambert's diffuse law of reflection:

$$G_{ij} \propto \frac{1}{\pi} \frac{\max(n_j \cdot u_I(t_i), 0) \max(n_j \cdot u_R(t_i), 0)}{\|r(t_i)\|^2}, \quad (10)$$

where  $u_I$  and  $u_R$  are the unitary vectors that point from the object to the illumination source (the Sun) and the observer (the telescope), respectively;  $r$  is the vector from observer to object;  $t_i$  is the instant of time of the corresponding  $L_i$ . Note that  $n_j$  and  $u_{\{I,R\}}$  must be all in the same frame. Therefore, it is necessary to know the attitude of the object at each time  $t_i$  as a rotation from inertial to body frame.

### 2.3 Light Curve to EGI

The simplest approach to recover an EGI from a diverse-enough light curve is to pre-define the number of directions  $N_a$  and the directions themselves  $\{n_j\}$  that shall be used to construct the EGI, and then use the model from Eq. 9 in a least squares problem to estimate the corresponding vector  $a$ . This is

$$\min_a \|L - Ga\|^2, \quad (11)$$

where here  $L$  is the measured light curve, while  $Ga$  is the estimated one.

<sup>1</sup>Although light is reflected as a photon flux, this text assumes a CCD detector that counts photons as detached electrons, hence the usage of the term *electron* flux.

### 2.3.1 Positivity of $a$

This regression should be bound so that  $a > 0$ , because a negative albedo-area has no physical meaning. There are different approaches by which this condition can be achieved.

- Kaasalainen and Torppa [12] suggest, for the application of this method on asteroid shape recovery, to substitute  $a_j$  by  $\exp(b_j)$ , and then optimize for  $b = [b_1, \dots, b_{N_a}]^T$ . This renders the least squares non-linear, which then they solve using the conjugate gradient method. Optimizing for unlimited  $b$  naturally guarantees positive  $a$ . Furthermore, the exponential function being bijective grants that a unique minimum of  $J$  in  $b$  corresponds to the same minimum in  $a$ .
- For use with artificial satellites, Calef *et al.* [3] and Fan and Früh [6] use constrained optimization directly on  $a$ . This paper employs the Non-Negative linear Least Squares (NNLS) method used in [6].

### 2.3.2 Convexity of the Recovered EGI

If the Recovered EGI is to be translated into a unique convex polyhedron, the convexity condition expressed by Eq. 4 has to be observed. However, the optimal solution to Eq. 11 does not necessarily comply with this condition. The possible reasons may be noise in the measurement [5, 6] or uncertainty in the model. The latter may come from different sources:

- First, the assumptions used to construct  $G$  (*i.e.* reflective model, attitude, etc.) may not match the observed object closely enough.
- Second, the tessellation scheme used to generate the EGI may miss important faces from the observed object, which causes deviations on the convexity condition.
- Third, albedo variegation may cause the recovered EGI not to represent a convex shape, because the varying albedos of the different faces of the object deform the  $a$  vector out of convexity [12].
- Finally, noise and biases in the light curve can cause the convexity residual to be non-zero.

In SPOOK, deviations from convexity are corrected by using a simple least squares solution of the problem [18]

$$\begin{aligned} \min_{a^*} \quad & J = \|\hat{a} - a^*\|^2, \\ \text{subj. to} \quad & \sum_{j=1}^{N_a} n_j a_j^* = 0. \end{aligned} \quad (12)$$

Thus,  $a^*$  is the closest approximation to the unconstrained albedo-areas solution  $\hat{a}$  in the least squares sense that, at the same time, lies within the subspace where Eq. 4 is true. Although forcing this constraint ensures the stability of the Malinowski minimization, it may add unwanted biases to the final solution. Kaasalainen and Torpa [12] use regularization directly on Eq. 11 to enforce this condition, while Fan and Früh [7] use the approach presented here, but with a lower bound  $a_j^* \geq \hat{a}_j$  together with a parameterizable upper bound.

### 2.3.3 Stability against Noise

To guarantee enough detail on the recovered shape, it is necessary to sample the EGI on the unit sphere with a tessellation scheme that is dense enough [8]. However, the computational cost of the Minkowski minimization problem increases with the number of directions of the EGI.

Nonetheless, due to noise in the signal and numerical errors, in practice EGIs recovered from light curves may present a relatively high number of small, non-zero values. These destabilize the Minkowski minimization process [3], and can be mitigated in different ways. Fan and Früh [6] do so by artificially zeroing all albedo-area values below a certain

threshold. Furthermore, they deal with noisy light curves by employing two separate consecutive light-curves [6] or by wrapping the shape inversion process in a particle-filter-based estimator using importance resampling [7]. Calef *et al.* [3] use Tikhonov (a.k.a. ridge) regularization,

$$\min_a J = \|L - Ga\|^2 + \alpha \|a\|, \quad (13)$$

and suggest a cross-validation scheme to choose the best value for  $\alpha$ . This paper proposes Lasso regularization

$$\min_a J = \|L - Ga\|^2 + \alpha \sum_{j=1}^{N_a} |a_j| \quad (14)$$

to help reduce noise sensitivity, too, because of its sharpening properties<sup>2</sup> – artificial objects are likely to have less, bigger faces than *e.g.* asteroids, with sharper edges.

## 2.4 Observability Conditions

Friedman and Früh [8] studied the observability of the inversion problem based on the Gramian of  $G$ , *i.e.*  $Q = G^T G$ . The unconstrained (negative values allowed) solution to the problem stated by Eq. 11 has a closed form given by

$$\hat{a} = Q^{-1} G^T L. \quad (15)$$

Thus, they define the observability of the problem by requiring that  $Q$  is invertible – *i.e.* that it has full rank.

However, the problem is rarely solved using Eq. 15, because of the positivity restriction imposed on  $a$  (see Sec. 2.3.1). Therefore, the Gramian  $Q$  is only a qualitative measure of observability. When either the exponential or the constrained approach is used to force positivity, the solution to the problem has no closed form, and must be resolved using some iterative method. In particular, if the NNLS problem is solved using active-set method by Lawson and Hanson [16], Kim [15] proved that a unique solution for  $\hat{a}$  exists despite  $Q$  being rank-deficient w.r.t. the number of directions in the EGI.

This implies that, in the noise-free ideal case,  $Q$  does not need to be full rank, but just have its rank high enough to capture independent information from each of the actual flat faces that compose the shape of the object being observed. These, of course, are unknown beforehand, hence the need for a shape-inversion method. However, especially in the case of objects with sharp edges and mostly flat faces, one shall expect that most directions in the EGI have zero albedo-area, while only a few have significant values. Therefore, for most artificial objects, indeed a considerably reduced number of directions should suffice to describe a recognizable shape. Therefore, in the noise-free scenario, it is interesting to tessellate the unit sphere with as many cells as computationally feasible, because this will ensure that non-zero albedo-area values are located where the normal is closest to that of the corresponding real face of the observed object.

When noise is present, however, the rank-deficient  $Q$  case can still work, but increasing the dependent dimensions too much can lead to instability due to high sensitivity to noise [3]. In these cases, the noise stabilization methods mentioned above [3, 6, 7] should be used.

## 3. SIMULATION SCENARIOS

The SPOOK implementation of the shape inversion from light curves using the EGI plus Minkowski minimization method has been tested with different shapes, noise scenarios and ranks of the problem Gramian.

### 3.1 Homotheticity Distance

To assess the success of each inversion, we have developed a technique to evaluate how close two distinct polyhedrons are, based on the homotheticity criterion. As defined in [18]:

**Definition 3.** Two 3D polyhedrons  $P$  and  $Q$  are **homothetic** if there exist  $s \in \mathbb{R}^+$  and  $t \in \mathbb{R}^3$  such that

$$P = \{x | x = sy + t, y \in Q\}, \quad (16)$$

---

<sup>2</sup>More on the results section.

Thus, to test the closeness of two polyhedrons, we want check how far from homotheticity they are.

To do so, we first define the remnant volume operation  $\Delta V(P, Q)$  between two polyhedrons  $P$  and  $Q$ , as the volume of the exclusive logical or ( $\vee$ ) between  $P$  and  $Q$ :

$$\Delta V(P, Q) := V(P \vee Q) = V(P) + V(Q) - 2V(P \wedge Q), \quad (17)$$

where  $\wedge$  represents the polyhedron clipping intersection and  $V(P)$  is a function that returns the volume of  $P$ . Given two convex polyhedrons defined by their limiting planes, the intersection can be easily computed *e.g.* by clipping and capping [1].

Then, we define the homotheticity distance as

$$H(P, Q) = \min_{s, t} \Delta V(P, T(Q, s, t)), \quad (18)$$

where  $T(Q, s, t)$  scales  $Q$  isotropically by the factor  $s$  and translates it by the vector  $t$ , as in Eq.16. In words, this *the homotheticity distance is the volume remnant of  $P$  and  $Q^*$ , where  $Q^*$  is scaled and translated from  $Q$  so that  $\Delta V(P, Q^*)$  is minimum.* The homotheticity distance of two homothetic polyhedrons is 0 – it complies with  $H(P, T(P, s, t)) = 0$  for any  $s$  and  $t$ .

To be able to compare different target shapes,  $H(P, Q)$  is normalized by the volume of the  $P$ ,

$$\bar{H}(P, Q) := \frac{H(P, Q)}{V(P)}. \quad (19)$$

### 3.2 Test Shapes

The shapes being tested are:

- a cube with 4 m side – it represents one of the simplest shapes achievable;
- an icosahedron with 1 m edges – it represents a slightly more complex, approximately spherical bus;
- a cylinder with 10 m length and 1 m radius – analogous to a simplified rocket body; and
- a winged cuboid, whose base is a 4 m × 6 m × 12.5 m cuboid and whose wings on either side are 6 m × 9 m rectangles without thickness, separated 1 m from the base – it emulates a non-convex object with solar panels.

Fig. 2 illustrates these shapes in orthographic projection, conserving the aspect ratio of each shape. Fig. 3 shows an example of the corresponding  $d = 5$  EGI for each shape, both in orthographic and Hammer projections. The color code represents the area of each cell, as indicated by the color bars. Cell borders are shown as white lines. Additionally, the latitude/longitude grid is shown in red on the Hammer projections.

Note that for the specific case of the winged cuboid, which is a non-convex shape, the EGI is generated by assuming that each face is not obscured along its normal by any other face. Because the thickness of the wings is null in the simulation, this assumption does not introduce any error. However, the EGI to polyhedron algorithm presented above recovers a convex shape instead (See the results section).

### 3.3 Scenario Geometry

The simulated light curve is measured by a telescope in the location of the Airbus Robotic Telescope (ART) [24] between 22:00 UTC of 2019-01-01 and 3:45 UTC of the following day. The simulated object always has the same circular Medium Earth Orbit (MEO) with 26731 km semi-major axis, 40° inclination and 10.94° right ascension of the ascending node. At midnight UTC of the observation night, it has a true anomaly of 67.5°. All test cases exhibit a nutation, the motion typical of a body with axial symmetry<sup>3</sup> whose angular momentum is constant and parallel to the inertial z-axis, with an overall magnitude of the angular rate of 3.44 min<sup>-1</sup>, nutating with the body z-axis at 70.5° from the angular momentum, at a rate of 2.7 min<sup>-1</sup>. Fig. 4 shows the simulated light curve for each test shape: in orange, the light curve without noise; in blue, the light curve randomized with SNR = 10 (see sub-section about measurement noise below). Circles are data points, and the lines are guides to the eye.

<sup>3</sup>Although some of the shapes introduced above do not present axial symmetry, during the simulations we have forced the same attitude profile to all of them, to remove the attitude as an added factor of comparison.

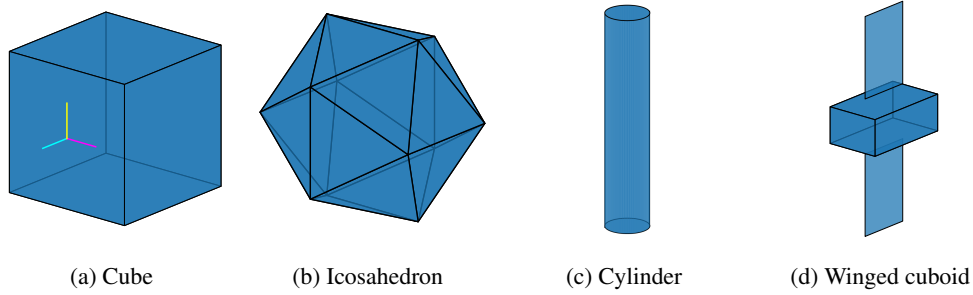


Fig. 2: Test shapes, body-frame axis represented in the Cube (cyan is  $x$ , magenta is  $y$  and yellow is  $z$ )

### 3.4 Light Curve Measurement

The light curves are modeled using the model from Sec. 2.2. Different noise conditions have been simulated, using the SPOOK light curve simulating capabilities [25]. Source and sensor noise is added from a Gaussian distribution, based on the median signal level represented by a Signal to Noise Ratio (SNR). This is, the measured light curve  $L = [L_1 \cdots L_{N_t}]^T$  is obtained by polluting each simulated value with additive noise:

$$L_i = L_i^s + \mathcal{N}\left(0, \frac{\bar{L}}{\text{SNR}}\right), \quad (20)$$

where  $L^s$  is a noise-less simulated value, and  $\bar{L}$  indicates the median of  $L^s$ . Fig. 4 shows an example noisy light curve with  $\text{SNR} = 10$  (blue) along its no-noise counterpart (orange), for each test shape.

### 3.5 Observability Conditions

This paper explores the shape recovery performance at different light curve sampling intervals (which affects the rank of the observability Gramian) and different EGI quad-tesselation divisions ( $d$  parameter). For the results in these paper, the light curve has been sampled at  $N_t \in \{150, 1000\}$  points, while the EGIs have been divided with  $d \in \{3, 5, 7, 9\}$ . The light curves from Fig. 4 are sampled at  $N_t = 1000$ .

### 3.6 Noise threshold

Following the technique used in [6] and companion papers, in this simulation the directions of the EGI with an area lower than  $\varepsilon \max(\hat{a})$  are ignored. This adds stability to the Minkowski minimization and filters out small area values that arise most likely from noise only. Then only those directions that survive this criterion are constrained for convexity with Eq. 12. This paper uses the value of  $\varepsilon = 5\%$ .

## 4. RESULTS AND DISCUSSION

This section presents and discusses the results of the shape recovery algorithm applied to the simulation scenarios described in the previous section. First, Tab. 1 shows the rank of the Gramian for each of the tested scenarios, which mainly depends on the number of cells of the EGI ( $N_a = 6d^2$ ) and the number of samples in the input light curve ( $N_t$ ). For all the cases tested, the numeric estimation of the rank always agrees with

$$\text{rank}(G^T G) = \min(N_a, N_t), \quad (21)$$

which means that the corresponding light curves have no redundant samples. In Tab. 1, rank-deficient scenarios – *i.e.*  $N_a < \text{rank}(G^T G)$  – are highlighted in **red**.

### 4.1 Cube

Starting with the cube shaped object, Fig. 5 shows the normalized homotheticity distance  $\bar{H}(P, \hat{P})$  as in Eq. 19 versus SNR, along different scenarios.  $P$  is the original polyhedron (the cube, in this case), and  $\hat{P}$  is the estimated one. Each plot corresponds to a light curve sampling density ( $N_t$ ). Each line corresponds to a specific EGI sampling  $d$ , color

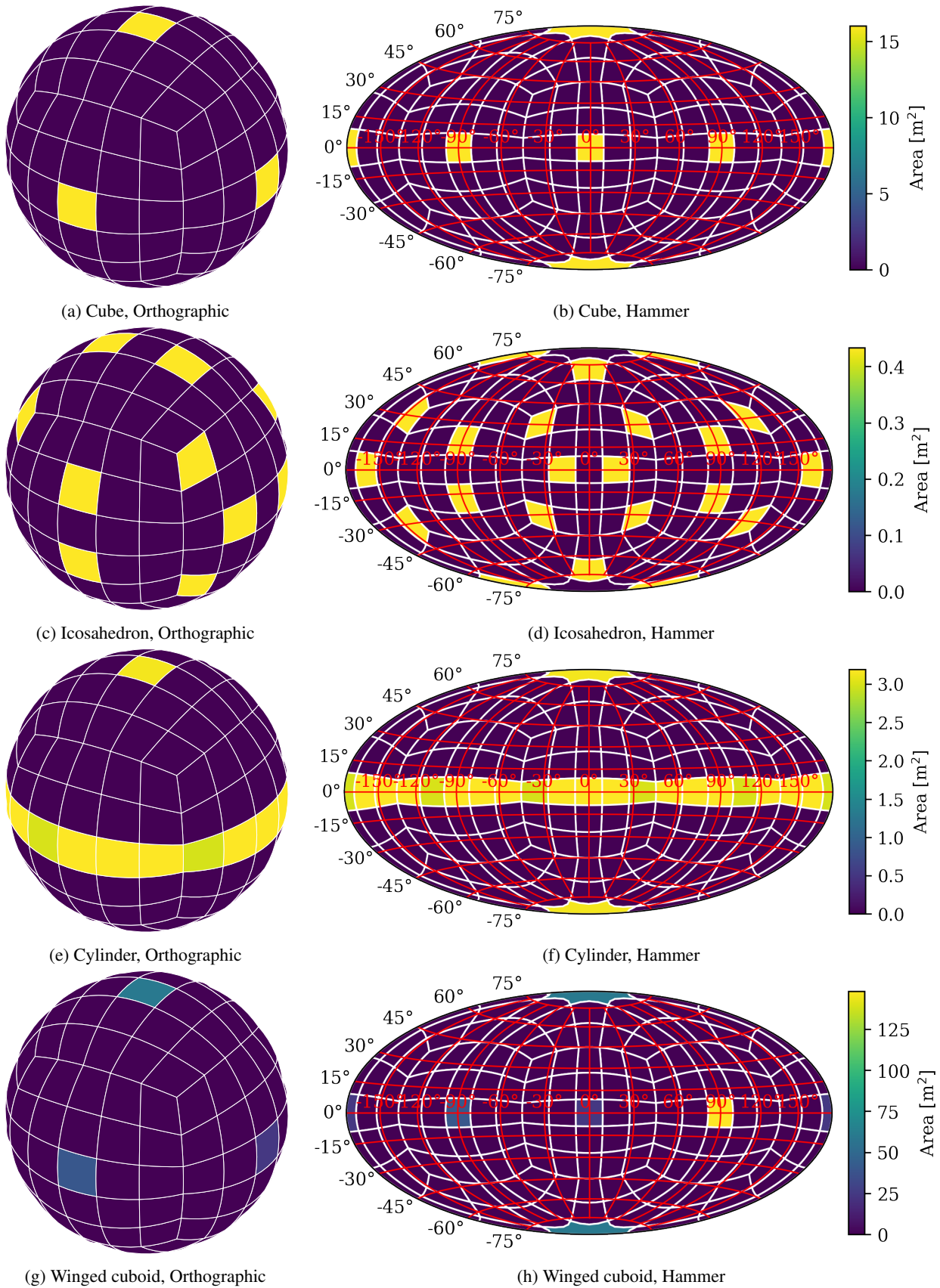


Fig. 3: EGIs of the test shapes, based on a  $d = 5$  quad-cube tessellation

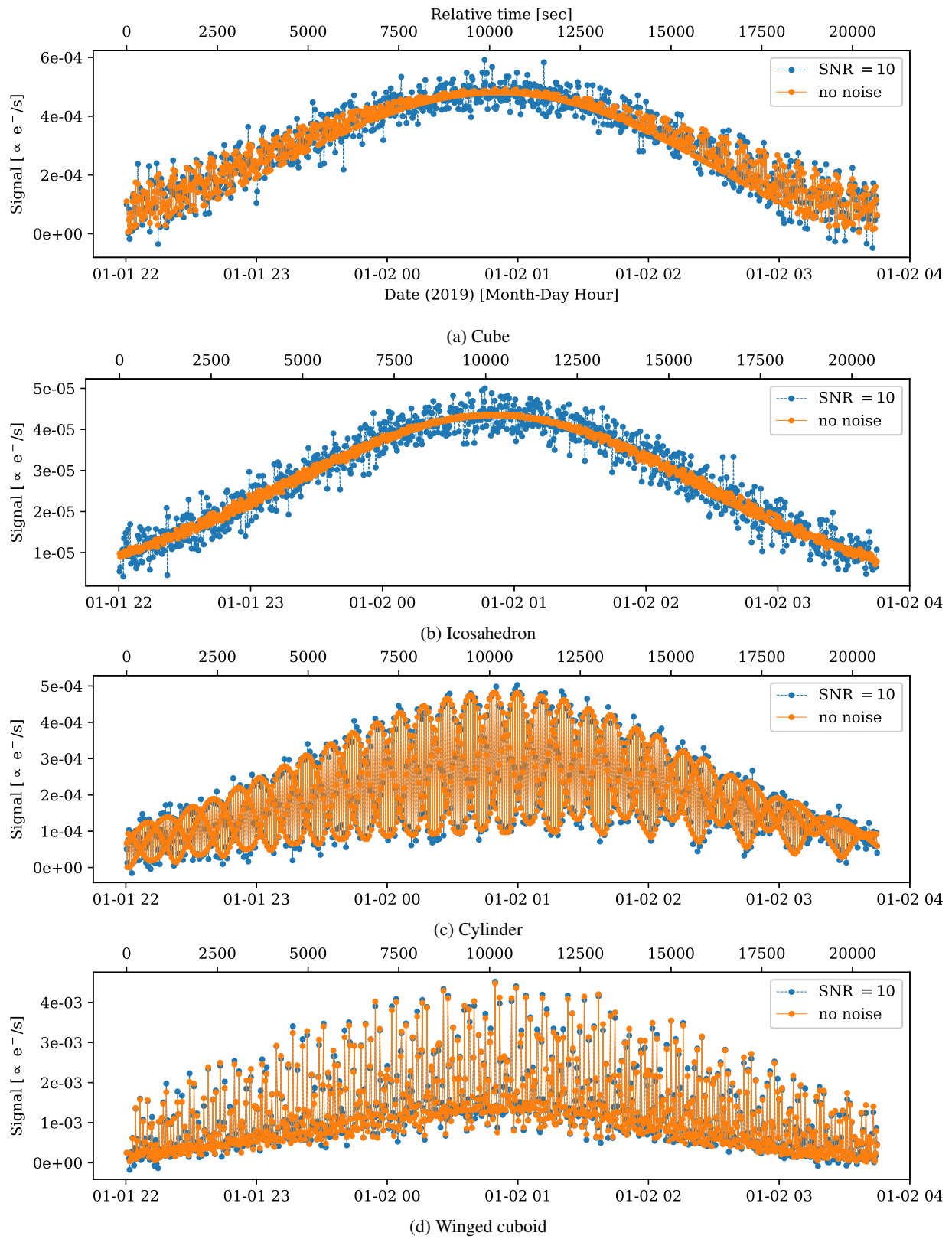


Fig. 4: Simulated light curves

Table 1: Rank of the Gramian ( $G^T G$ ) at different light curve and EGI sampling densities

$d$	$N_a$	rank( $G^T G$ )	
		$N_l = 150$	$N_l = 1000$
3	54	54	54
5	150	150	150
7	294	150	294
9	486	150	1000

coded. Each (SNR,  $\bar{H}$ ) point ( $\times$ ) on the plots is the result of averaging the individual performance over  $N_{MC} = 64$  runs within a Monte Carlo simulation, where the noise is randomly sampled according to Eq. 20 at each run. This is

$$\hat{\mu} = \frac{1}{N_{MC}} \sum_{i=1}^{N_{MC}} \bar{H}(P, \hat{P}_i). \quad (22)$$

The vertical bars delimited by opposite triangles indicate the  $\sim 95\%$  confidence interval of  $\hat{\mu}$ , computed from the unbiased estimation of the standard deviation:

$$s^2 = \frac{1}{N_{MC} - 1} \sum_{i=1}^{N_{MC}} (\bar{H}(P, \hat{P}_i) - \hat{\mu})^2. \quad (23)$$

To estimate these error bars, we have assumed the normality of  $\hat{\mu}_{\bar{H}}$ . Thus, they span over the range

$$-1.96 \frac{s}{N_{MC}} < \bar{H} - \hat{\mu} < 1.96 \frac{s}{N_{MC}}. \quad (24)$$

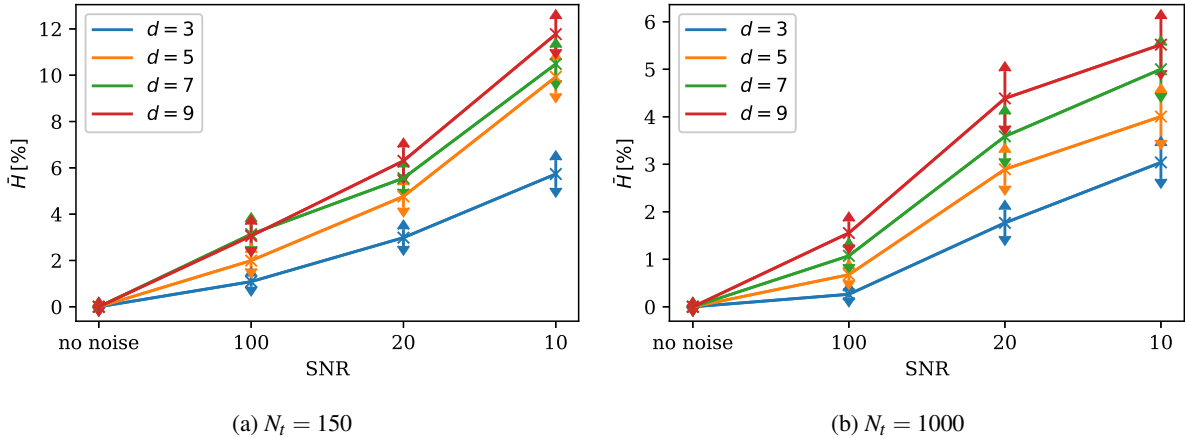


Fig. 5: Cube results, averaged over 64 Monte Carlo runs

For the *no noise* case, the shape can be recovered with maximum fidelity ( $\bar{H} = 0$ ), even when the Gramian is rank-deficient. This stems from two main factors. First, both light curves ( $N_l = \{150, 1000\}$ ) have enough samples, and come from a wide enough range of attitude states, so that the six faces of the cube are observable. Second, all the quad-cube tessellation sizes have one cell aligned to each of the six faces of the cube. Thus, all the important information goes there, and the rest of the cells are virtually zero – they do not capture any significant amount of area-albedo that could *e.g.* affect the shape recovery differently for different values of  $N_l$  or  $d$ .

Moving over to the noisy scenarios shown on Fig. 5, the first noticeable point is that fidelity decreases with higher SNR values, as expected. Unsurprisingly, the scenario with the denser light curve produces better fidelity – more samples implies more information on the object. Regarding the effect of  $d$  (or  $N_a$ ), Fig. 5 shows that, for the cube, a denser EGI always leads to higher error. Moreover, this trend does not seem to be highly influenced by whether the scenario

is rank-deficient or not. This may again be explained by the affinity of the cube to the quad-cube tessellation: because the  $d = 1$  EGI is enough to perfectly capture its six faces, more cells than these are just recipients to be populated by noise, each of which contributes further to fidelity error on the recovered shape.

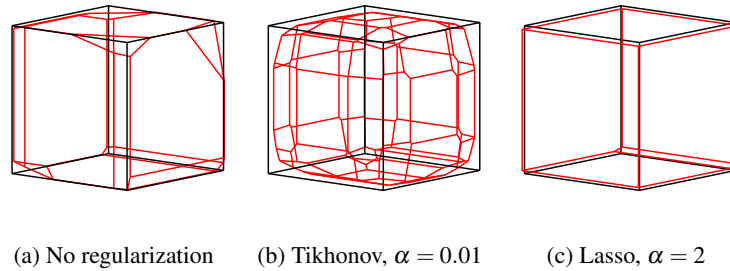


Fig. 6: Original (black) versus recovered (red) shape for the cube

The cube being the simplest shape on the test bench, has been chosen to qualitatively assess the effects that regularization can have on the recovered shape. While Tikhonov (Eq. 13) regularization favors many smaller values in the estimated parameter vector, Lasso (Eq. 14) regularization encourages a sparser parameter vector, with a few big values and the rest almost null. Thus, when recovering an EGI from a light curve

- shapes estimated using Tikhonov regularization tend to be more rounded, compared to not using regularization, because the area from big area cells *flows* into neighboring ones. In contrast,
- when using Lasso regularization, shapes have fewer faces and sharper edges, because neighboring cells with similar area values tend to merge into a single cell with bigger area.

This expected behavior can be observed in Fig 6, where the original (black-edged frame) and recovered (red-edged frame) for three solutions with different regularization schemes are shown, in the scenario of  $N_l = 1000$ ,  $d = 7$  and  $\text{SNR} = 10$ , for one random Monte Carlo run. The values of  $\alpha$  have been manually tuned to exemplify the features of each regularization scheme. However, as suggested in [3], a more rigorous approach would be to use a cross-validation scheme to choose the ideal value of  $\alpha$ . Qualitatively, Fig 6 shows that the non-regularized shape has some apparently random deviations from the cube; the Tikhonov solution smooths them out by rounding the edges, while the Lasso one removes them by adding them to the biggest faces. In this case, because the cube is a clear example of a shape with a few big faces, Lasso clearly outperforms the other approaches.

## 4.2 Icosahedron

The next shape on the test bed is the icosahedron, whose results are shown in Fig.7 (see Sec. 4.1 for a detailed explanation of the plots).

As happened with the cube, with the icosahedron fidelity error increases with higher noise levels (SNR) and sparser light curves ( $N_l$ ). However, it differs from the cube in other aspects. First, with the icosahedron case one does not recover an exact replica of the original shape (*i.e.*  $\bar{H} = 0$ ) even in the *no noise* scenarios. This is because the normals of the faces of the icosahedron are not aligned with any particular direction of the quad-cube tessellation. Thus, we can see that, for the *no noise* scenarios, the fidelity improves with a denser EGI, *even when the Gramian is rank-deficient*. This happens because, for a denser EGI, the closest direction to each normal of the icosahedron will be closer to it. Thus, the denser EGIs approximate the icosahedron faces better. For this same reason, at low noise levels (SNR = 100) denser EGIs still perform better. However, for the noisiest cases (SNR = 10), noise dominates and the EGI density has no significant impact anymore.

The Icosahedron plot presents some points where the error bars are unusually wide. These are  $d = 7$ , SNR = 20 on the  $N_l = 150$  light curve, and  $d = \{7, 9\}$ , SNR = 20 for  $N_l = 1000$ . This may indicate some instability in the shape recovery process that produces higher variance homotheticity distance measurements, which should be investigated further with a wider range of scenarios – *e.g.* varying noise threshold ( $\epsilon$ ) values.

Regarding regularization, the icosahedron has also been tested qualitatively, for the same scenario as the cube (see previous section). Fig 8 shows the corresponding results. Opposite to the cube, the icosahedron has more faces with

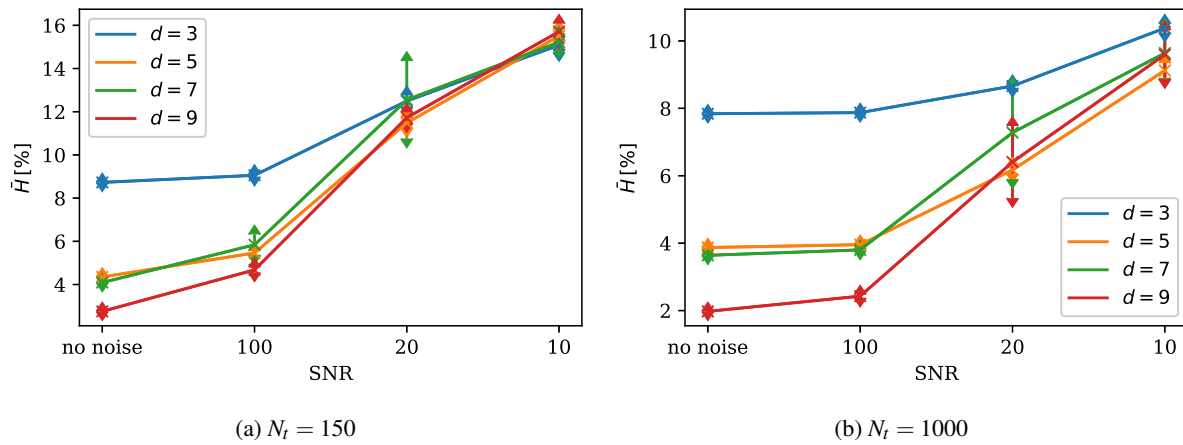


Fig. 7: Icosahedron results, averaged over 64 Monte Carlo runs

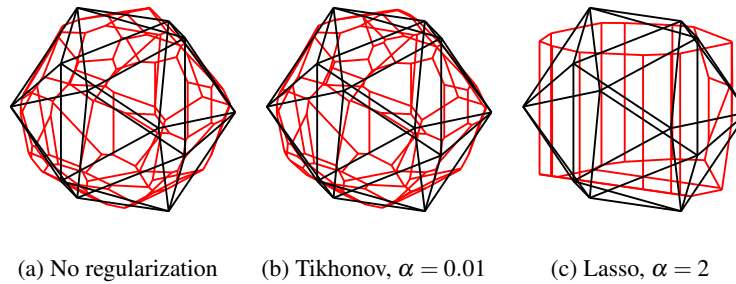


Fig. 8: Original (black) versus recovered (red) shape for the icosahedron

less area. As a consequence, the non-regularized and the Tikhonov schemes barely differ: the non-regularized solution is already quite rounded, so ridge regularization has little effect on it. On the contrary, the Lasso regularization with the same high value of  $\alpha$  as in the cube case completely distorts the recovered shape away from the icosahedron – lower values of  $\alpha$  for the Lasso scheme do not produce important changes w.r.t. the non-regularized case. Thus, the icosahedron is a good counter example to the regularization results of the cube.

### 4.3 Cylinder

The last convex shape tested in this paper, the cylinder, has its results in Fig. 9 (see Sec. 4.1 for a detailed explanation of the plots).

In contrast to the two previous shapes, it has proven to be much more difficult to recover:  $\bar{H}(P, \hat{P})$  is greater overall. This is probably due to the cylinder having a smooth curvature, which contradicts (or at least strains) the hypothesis of a shape represented by a polyhedron build from several flat faces – the side of the cylinder is the limit of infinite faces with infinitesimal area. Beyond this point, the effects of  $N_t$  and  $SNR$  share the same trends as with the cube and icosahedron cases: higher  $N_t$  and higher  $SNR$  improve fidelity, as is to be expected.

For the *no noise* cases, there is no clear trend whether denser EGIs perform better or not, although for  $N_t = 150$  it seems that rank-deficient cases perform slightly worse. Instead, moving to the noisy scenarios, as noise level increases, denser EGIs clearly deteriorate fidelity, regardless of the rank of the Gramian – as with the cube. In fact, the two circles of the cylinder do match the polar faces of a quad-cube tessellation with an odd value of  $d$ , while its sides all map more or less well to the cells in the equator of the quad-cube. Thus, although the match is not as close as with the cube, it is plausible that the cylinder maps onto a low  $d$  quad-cube well enough so that the potential benefits of higher density are overrun by a wider spread of noise. This is, the cylinder is better approximated by a cleaner prism whose base is a polygon of less vertices, than one whose base has more vertices but is rougher.

Fig. 11 shows the original (black-edged frame) and recovered (red-edged frame) shapes for the cylinder case, for

$N_t = 100$ ,  $d = 7$  and  $\text{SNR} = 10$ , an arbitrary Monte Carlo run. A common feature with most of its iterations, is that the recovered shape is shorter along the cylinder axis, but wider orthogonality. This agrees with the conjecture that information is lost due to the real cylinder having infinite flat faces on its sides that are infinitesimally small, hence the axial shortness. Nonetheless, the recovered shape clearly resembles a cylinder.

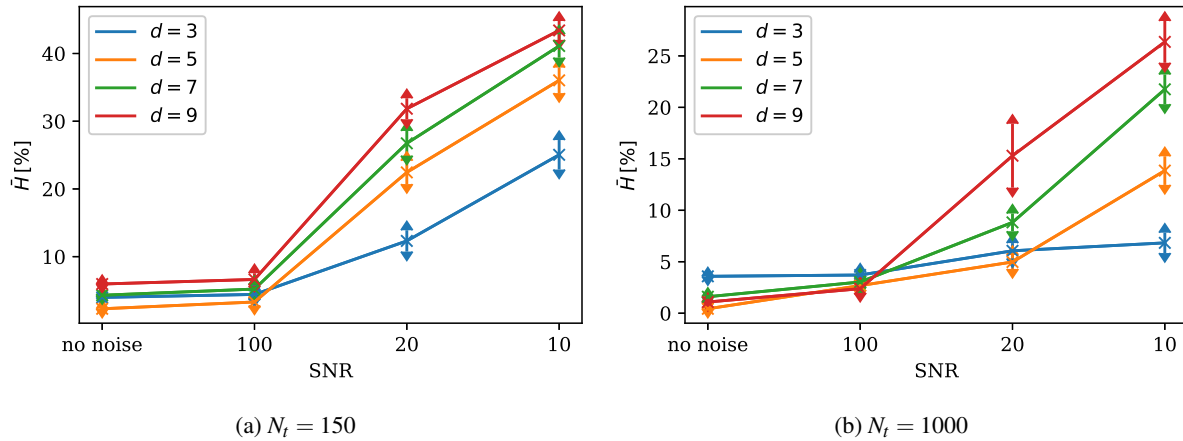


Fig. 9: Cylinder results, averaged over 64 Monte Carlo runs



Fig. 10: Original (black) versus recovered (red) shape for the cylinder

#### 4.4 Winged Cuboid

The winged cuboid is a non-convex object. As such, it cannot be uniquely represented by an EGI, as per Minkowski’s theorem [19]. Nonetheless, it is still possible to recover an EGI from its light curve. In fact, in the particular case of the winged cuboid, for the  $N_t = 100$ ,  $d = 7$  and  $\text{SNR} \rightarrow \infty$  scenario, the area residual is  $4.29e - 03$ , low enough to pass as a convex object. In other words, Minkowski’s minimization can be applied to recover an *equivalent* convex shape – *i.e.* the shape that would produce a light curve as similar as possible to the measured one [12]. This recovered shape may be significantly different than the original one, however. Fig. 11 shows the original (black-edged frame) and recovered (red-edged frame) shapes for the winged case, for  $N_t = 100$ ,  $d = 7$  and  $\text{SNR} = 10$ .

Minkowski’s minimization only renders convex shapes, hence the recovered shape approximates a cuboid that significantly far away from the original winged cuboid. Its only similitude is the ratio of cross section areas in any two different observation directions is approximately equal when calculated for the original or for the recovered shape – this is a necessary condition if the recovered shape has to reproduce the measured light curve as faithfully as possible. Despite this, the two shapes are clearly far from homothetic. For this reason, a wide range of tests to assess the impact  $N_t$ ,  $d$  and  $\text{SNR}$  on the homotheticity distance of original and recovered polyhedron has not been performed within the scope of this paper.

Nonetheless, this experiment shows that *equivalent* convex shapes can be recovered even for non-convex objects. These could be used to help identify, classify or simulate the light curves of these objects, even if the *equivalent* convex shape is far from the original shape of the object.

Another important conclusion from this experiment is that the recovered shape is highly dissimilar from the convex hull of the original shape, even if scaled, which differs from the results presented in [12], where recovered shapes of

asteroid-like non-convex bodies were found to be close to the corresponding convex hulls. This is an extreme example of the conclusion therein, which states that the greater the concavities in the original object, the farther the *equivalent* convex shape is from the convex hull.

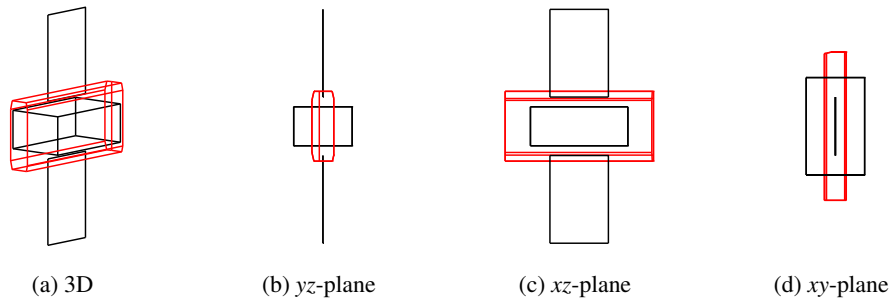


Fig. 11: Original (black) versus recovered (red) shape for the winged cuboid

#### 4.5 General Discussion

This sub-section closes the results part of the paper by summarizing and merging the conclusions extracted from all the tested scenarios together.

Overall, regarding convex shapes, via Monte Carlo simulations of 64 runs each and evaluating the homotheticity distance, it has been shown that

- the sampling density of a light curve (which *observes* the object in a varied enough range of observation geometries),
- the density of the EGI and
- the noise level present in the light curve

have a strong impact on the shape inversion results. Light curve sampling density and noise level have the expected impact on the results: more samples and less noise means better results. However, depending on the studied shape, denser or sparser EGIs can perform better. It has been conjectured that the main reason is the affinity/dissimilitude of the real shape and the quad-cube tessellation scheme. Further studies should investigate whether different tessellation schemes, such as the geodesic dome proposed in [3, 11], lead to significantly different performance curves – *e.g.* the icosahedron would have more affinity with an icosahedron-based geodesic dome. The rank-deficiency/fullness of the Gramian of the problem has been found to have a marginal impact, significantly lower than the other aforementioned parameters: similar trends are observed with  $N_t = 150$ , where half of the cases are rank-deficient, and with  $N_t = 1000$ , where all cases are full-rank.

Still on convex shapes, regarding regularization, it has been shown qualitatively that Lasso stabilizes noisy scenarios for shapes with few, big faces, while Thikhonov is better suited for naturally rounder shapes. However, care must be used when applying regularization. Both Lasso and ridge smooth the parameter vector by adding some bias (sharper/rounder features). For objects with *a priori* unknown shapes, it is not possible to know if it is better to sharpen or to round the noisy recovered shape. Thus, it is not known if the added bias corrects or further deforms the result. All in all, regularization should only be used if some *a priori* information on the general shape of the object is known beforehand – *e.g.* it is likely that asteroids are rounder, hence ridge may improve smoother sharp features that originate from noise.

### 5. POTENTIAL EXTENSIONS

This section discusses possible extensions to recover additional information, or to improve the results of the shape inversion method based on EGI estimation plus Minkowski's minimization.

## 5.1 Albedo Variiegation

For the case of asteroids, Kaasalainen and Torppa [12] propose a regularization scheme in which they minimize the albedo and area as separate terms so that, when multiplied element-wise, they are equal to the obtained  $\hat{a}$ . To constrain the infinite-solutions problem, they add two regularization components, one for the convexity condition, and one that describes how albedo should vary across the surface of the object.

In the case of asteroids, although albedo distributions are typically unknown, they in general can be assumed to be smooth enough across different regions of the asteroid. Therefore, it is plausible to use some constraint that penalizes fast albedo variations in any direction along the surface [12]. Man-made objects, however, cannot be expected to have constant or smooth albedo distributions; on the contrary, one should expect artificial satellites to have external components with radically different optical properties (*e.g.* solar panel vs. antenna dish vs. multi-layer insulation). This means that, unless *a priori* information on the albedo distribution of the particular object is known, using single-channel<sup>4</sup> light curves the albedo-area separation for man-made objects is not possible.

## 5.2 Non-Convexity

As shown in this paper, the estimated *equivalent* convex shape of a non-convex object may share some characteristics with the original one, but has a great homotheticity distance and is, of course, convex. Kaasalainen and Torppa [12] managed to qualitatively characterize concavities in asteroid-like non-convex objects, not being able to fully recover the depth of the valleys, but only to infer their presence. They did so by modifying the vertices of the *equivalent* convex shape by a set of coefficients, which then they used to optimize, in the least squares sense, the difference between the measured light curve and the one obtained by simulating it with the candidate non-convex shape.

However, Viikinkoski *et al.* [26] argue that photometry data alone is not enough to determine a non-convex shape uniquely: one big concavity can be replaced by a set of smaller concavities that produce the same light curve signature. Thus, non-convex shape recovery must involve other types of measurements, which constrain the possible shape enough to overcome the non-uniqueness of the problem: in [14], it is shown that low resolution images that provide a rough contour of cross-sections of the object can help toward this goal.

## 5.3 Attitude Estimation

The most appealing extension of the shape inversion method, would be to couple it with simultaneous attitude estimation, based solely on photometry (light curves). This would allow the full characterization of an object for which no *a priori* information exists. However, except for particular cases where some constraints can be applied [9, 12, 25], this is an unsolved problem so far due to observability constraints.

As in the non-convex case, resolved imagery or other complementary data sources have the highest potential to make the coupled problem observable, allowing to estimate both shape and attitude at the same time.

## 6. CONCLUSION

This paper has demonstrated how SPOOK can estimate the (*equivalent* convex) shape of an orbiting object, for which the attitude profile and orbit are known. It has used SPOOK's own measurement simulation layer to generate the necessary light curves in a variety of scenarios, including different noise levels and test shapes. Performance of the shape inversion has been assessed based on the *homotheticity distance*, a quantity defined in this paper for the first time. The results shown indicate that SPOOK can recover the shapes of convex objects with acceptable fidelity, as long as the light curves are long and dense enough, even for high noise cases.

Finally, potential extensions to albedo, non-convexity and attitude estimation have been briefly discussed, and remain open points for further iterations.

The next step would be to use the Airbus Robotic Telescope to obtain good quality light curves of operated satellites whose telemetry is known, so that attitude is an input, and test the shape inversion on them. This would stress the method further, although problems such as albedo variegation and non-convexity would still have to be addressed.

---

<sup>4</sup>By single channel, we mean light curves measured with a single sensor, at a specific single (color) band. In contrast, multiple channel light curves are simultaneous light curves of the same object, from the same location, observed through different bands.

## 7. ACKNOWLEDGMENTS

The first author would like to thank Nils Frederik Hasselmann for his counsel on the presentation of results.

## 8. REFERENCES

- [1] H. T. Ahn and M. Shashkov. Geometric algorithms for 3D interface reconstruction. In M. L. Brewer and D. Marcum, editors, *Proceedings of the 16th International Meshing Roundtable*, pages 405–422, Berlin, Heidelberg, Springer Berlin Heidelberg, 2008.
- [2] R. H. Byrd, M. E. Hribar, and J. Nocedal. An Interior Point Algorithm for Large-Scale Nonlinear Programming. *SIAM Journal on Optimization*, 9(4):877–900, 1999.
- [3] B. Calef, J. Africano, B. Birge, et al. Photometric signature inversion. In V. L. Gamiz, P. S. Idell, and M. S. Strojnik, editors, *Unconventional Imaging II*, volume 6307, pages 141–150. International Society for Optics and Photonics, SPIE, 2006.
- [4] ESA’s Annual Space Environment Report. GEN-DB-LOG-00288-OPS-SD, ESA Space Debris Office, 2021. (Visited on 08/23/2021).
- [5] S. Fan, A. Friedman, and C. Frueh. Satellite Shape Recovery from Light Curves with Noise. In S. Ryan, editor, *Advanced Maui Optical and Space Surveillance Technologies Conference*, 2019.
- [6] S. Fan and C. Frueh. A Direct Light Curve Inversion Scheme in the Presence of Measurement Noise. *The Journal of the Astronautical Sciences*, 67(2):740–761, 2020.
- [7] S. Fan and C. Frueh. Multi-Hypothesis Light Curve Inversion Scheme for Convex Objects with Minimal Observations. In 8th European Conference on Space Debris. ESA Space Debris Office, 2021.
- [8] A. Friedman, S. Fan, C. Frueh, et al. Observability of Light Curve Shape Inversion Based on Optical Data. In First International Orbital Debris Conference, 2019.
- [9] D. Hall and P. Kervin. Optical characterization of deep-space object rotation states. In *Advanced Maui Optical and Space Surveillance Technologies Conference*, 2014.
- [10] M. J. Holzinger, K. T. Alfriend, C. J. Wetterer, et al. Photometric Attitude Estimation for Agile Space Objects with Shape Uncertainty. *Journal of Guidance, Control, and Dynamics*, 37(3):921–932, 2014.
- [11] B. K. P. Horn. Extended Gaussian Images. *IEEE*, 72(12):1671–1686, 1984.
- [12] M. Kaasalainen and J. Torppa. Optimization methods for asteroid lightcurve inversion. I. Shape determination. *Icarus*, 153(1):24–36, 2001.
- [13] M. Kaasalainen, J. Torppa, and J. Piironen. Models of Twenty Asteroids from Photometric Data. *Icarus*, 159(2):369–395, 2002.
- [14] M. Kaasalainen. Asteroid models from photometry and complementary data sources. In *AIP Conference Proceedings*, volume 1732 of 020003, 2016. eprint: <https://aip.scitation.org/doi/pdf/10.1063/1.4948806>.
- [15] J. Kim. *Nonnegative Matrix and Tensor Factorizations, Least Squares Problems, and Applications*. PhD thesis, Georgia Institute of Technology, Atlanta, Georgia, US, 2011. 145 pages.
- [16] C. L. Lawson and R. J. Hanson. *Solving Least Squares Problems*. Society for Industrial and Applied Mathematics, 1995. 351 pages.
- [17] E. Linder, J. Silha, T. Schildknecht, et al. Extraction of Spin Periods of Space Debris from Optical Light Curves. In *66th Astronautical Congress International*. Curran Associates, Inc., 2015.
- [18] J. J. Little. *Recovering Shape and Determining Attitude from Extended Gaussian Images*. PhD thesis, University of British Columbia, Vancouver, Canada, 1985. 93 pages.
- [19] H. Minkowski. Allgemeine lehrrätze über die convexen polyeder. *Nachrichten von der Gesellschaft der Wissenschaften zu Göttingen, Mathematisch-Physikalische Klasse*, 1897:198–220, 1897.

- [20] G. Pedone, D. Vallverdu Cabrera, M. G. Dimitrova Vesselinova, et al. SPOOK: a tool for space objects catalogue creation and maintenance supporting space safety and sustainability. In *7th Annual Space Traffic Management Conference*, 2021.
- [21] O. Rodriguez Fernandez, J. Utzmann, and U. Hugentobler. SPOOK - A Comprehensive Space Surveillance and Tracking Analysis Tool. In *7th European Conference for Aeronautics and Aerospace Sciences*, 2017.
- [22] O. Rodriguez Fernandez, J. Utzmann, and U. Hugentobler. Correlation of Optical Observations to Catalogued Objects using Multiple Hypothesis Filters. In *1st NEO and Debris Detection Conference*, 2019.
- [23] J. Torppa, M. Kaasalainen, T. Michałowski, et al. Shapes and rotational properties of thirty asteroids from photometric data. *Icarus*, 164(2):346–383, 2003.
- [24] J. Utzmann, M. G. Dimitrova Vesselinova, and O. Rodriguez Fernandez. Airbus Robotic Telescope. In *1st NEO and Debris Detection Conference*, 2019.
- [25] D. Vallverdu Cabrera, J. Utzmann, and R. Förstner. Integration of attitude characterization in a space debris catalogue using light curves. In *8th European Conference on Space Debris*. ESA Space Debris Office, 2021.
- [26] M. Viikinkoski, J. Hanuš, M. Kaasalainen, et al. Adaptive optics and lightcurve data of asteroids: twenty shape models and information content analysis. *Astronomy & Astrophysics*, 607:A117, 2017.
- [27] R. A. White and S. W. Stemwedel. The quadrilateralized spherical cube and quad-tree for all sky data. In D. M. Worrall, C. Biemesderfer, and J. Barnes, editors, *Astronomical Data Analysis Software and Systems I*, volume 25 of *Astronomical Society of the Pacific Conference Series*, page 379, 1992.